Materials Advances

ROYAL SOCIETY OF CHEMISTRY

PAPER

View Article Online
View Journal | View Issue

Cite this: *Mater. Adv.*, 2025, **6**, 8701

DFT insights into the gas sensing performance of M_2X (M = Zr, Hf; X = C, N) MXenes and their Janus derivatives for toxic gases

Muhitul Islam,[a] Siraj Ud Daula Shamim, *[a] Bivas Kumar Dash,[a] Aditi Ahmed Ananna,[a] Mohammad Sadiqur Rahman,[b] Tanu Arefin[c] and Afiya Akter Piya[a]

Received 31st May 2025,
Accepted 8th October 2025

DOI: 10.1039/d5ma00568j

rsc.li/materials-advances

Widespread air pollution caused by toxic, flammable, and hazardous gases has been linked to numerous health issues. Gas sensors play a crucial role in the detection and monitoring of these harmful substances. In this study, Zr and Hf-based carbide and nitride MXenes (Zr_2C, Zr_2N, Hf_2C, and Hf_2N) and their Janus structures (ZrHfC and ZrHfN) were investigated for their sensing performance towards the toxic CO, NO, NO_2, and SO_2 gas molecules using density functional theory (DFT). The adsorption behavior in terms of adsorption energy, charge transfer, recovery time, electronic properties in terms of band structures, density of states (DOS), and work function were examined to understand the sensing behavior of the nanosheets. Chemisorption interactions were found for all of the complexes except CO and SO_2 adsorption on ZrHfC. Favorable adsorption characteristics were observed for the CO and NO gases on all the nanosheets. The adsorption energies ranged from −1.65 to −3.37 eV for CO and −4.42 to −5.32 eV for NO, with corresponding Mulliken charge transfers of −0.152 to −1.00*e* and −0.172 to −1.038*e*, respectively. But in the case of NO_2 and SO_2, very high adsorption characteristics with high deformation of the gases in the complexes were found, which leads to unfavorable adsorption performances. Furthermore, the work functions of the nanosheets varied during the adsorption of gas molecules. Thus, all calculations indicate that all six nanosheets can be useful for monitoring CO and NO.

1. Introduction

The existence of hazardous gas molecules in the environment is increasing rapidly due to rapid industrialization, which is alarming for the environment. Hazardous, poisonous, combustible, and explosive gases such as ethanol (C_2H_6O), formaldehyde (HCHO), nitrogen oxides (NO_x), acetone (C_3H_6O), ammonia (NH_3), sulfur oxides (SO_x), and carbon monoxide (CO) pose serious threats to human health, environmental safety, and urban air quality and contribute significantly to carbon emissions and other global concerns. Toxic gases are the prime cause of cardiovascular diseases, cardiac dysfunction, nausea, acute headaches, respiratory issues, asthma, neural damage, and so on.[1,2] CO is a poisonous gas without smell, color, or taste. It forms when fuels such as wood, coal, or gas don't burn completely or when gas doesn't get enough fresh air. When inhaled, it binds to blood cells faster than oxygen, developing a lack of oxygen in the body and leading to tissue hypoxia, brain injury, or even death.[3] SO_2 is a colorless, corrosive, and highly irritant gas that can cause significant health effects. It causes bronchoconstriction in asthmatic subjects, exacerbates asthma, chronic bronchitis, and chronic obstructive pulmonary disease, and contributes to acid rain.[4] Nitric oxide (NO) and nitrogen dioxide (NO_2) are major air pollutants that harm both health and the environment by contributing to acid rain, ozone depletion, and the greenhouse effect.[5] Air contamination disturbs the natural atmospheric conditions and creates an ecological imbalance, resulting in 9 out of 10 people inhaling highly contaminated air, according to WHO.[6]

Researchers have concentrated on developing complex gas sensors that offer high accuracy and speed in detecting the concentrations of gases to enable the rapid identification of these gas molecules. These sensors have several applications, such as the detection of explosives, medical diagnostics, food and beverage quality evaluation, and air quality monitoring. Many two-dimensional (2D) nanomaterials, including phosphorene, graphene, related 2D crystals, and even MXenes, have been utilized as gas-sensing materials over the past few decades due to their ultrahigh surface area, strong exterior actions, high mobility, outstanding thermal and electrical conductivity

[a] *Department of Physics, Mawlana Bhashani Science and Technology University, Tangial-1902, Dhaka, Bangladesh. E-mail: sdshamim@mbstu.ac.bd*
[b] *Dhaka University of Engineering & Technology, Gazipur-1707, Bangladesh*
[c] *Department of Physics, Bangladesh University of Textiles, Dhaka-1208, Bangladesh*

values, and high chemical and thermodynamic durability.[7–9] A new class of two-dimensional materials called MXenes was discovered in 2011. It comprises nitrides, carbides, oxycarbides, and nitrocarbides of transition metals. These substances have generated considerable attention due to their various applications in energy storage, hydrogen generation, gas sensing, biological sensing catalysis, and water purification.[10,11] The structures are composed of 2–5 sections of initial metals that transition (M), linked with 1–4 stages of X (C or N) that can be prepared by eliminating ''A'' sections (including Al or Si) *via* MAX indicators and by employing non-MAX ones.[12] By taking out the ''A'' element from the bulk MAX phases, 2D MXene systems as suitable models were built.[13,14] For simplicity, the focus was placed on M_2X-type MXenes, the thinnest members of the MXene family, where M represents transition metals such as Sc, Ti, Zr, Hf, V, Nb, Ta, and Cr, and X stands for either carbon (C) or nitrogen (N). Finally, the overall findings were discussed on thicker MXene systems.[15–18] It is anticipated that the produced metal surfaces will undergo chemical termination following the removal of the ''A'' element.[13,19] When hydrofluoric acid (HF) acid solutions chemically exfoliate the MXenes, it has been observed experimentally that the exterior layers dissolve *via* F and/or OH groups.[20,21] Additionally, O-terminated surfaces could be created chemically or by post-processing OH-terminated systems, for example, by thermal treatment or an ultraviolet-ozone cleaning method.[19,22,23]

From Table 1, it is clear that most previous DFT investigation focused on single-component MXenes that were utilized for detecting various toxic gases. These studies reported good charge transfer and sensitivity. However, they did not investigate Janus or heterostructure MXenes and were mainly restricted to conventional MXenes. Furthermore, common defects in MXenes, such as vacancies or missing atoms, can significantly affect the gas sensing properties. They often create additional active sites, enhancing adsorption and charge transfer with gas molecules, which can improve sensitivity and selectivity. However, a high concentration of defects may reduce structural stability. In recent years, numerous theoretical investigations have reported promising gas sensing properties of Janus material transition metal dichalcogenides beyond MXenes. Therefore, in this work, we focused on Janus MXenes. For instance, H. Dou *et al.*[32] and B. Paul *et al.* explored Janus WSTe and WSeTe monolayers to determine toxic gases including CO, NO, and O_2, while L. Ju *et al.* demonstrated that Se-vacancies in Janus WSSe enhance sensitivity toward NO_2.[32–34] The selective adsorption of SO_2 and NO_2 on Janus MoSSe was also reported by B. Babariya *et al.*[35] Our exploration of Janus MXenes as novel gas sensing materials is further motivated by these works, which demonstrate how the intrinsic asymmetry of Janus structures can greatly enhance the gas sensing performance. Therefore, the current work depends on DFT to methodically investigate Hf_2C, Hf_2N, Zr_2C, Zr_2N, and their Janus heterostructures (ZrHfC and ZrHfN).

2. Computational details

Using the DMol^3 component in the Materials Studio software, DFT calculations were performed to investigate the interactions among six nanosheets and unique gas molecules, such as CO, NO, SO_2, and NO_2.[36,37] The exchange–correlation functions were analyzed using the GGA (generalized gradient approximation) with the Perdew–Burke–Ernzerhof (PBE) approach.[36] To adjust for relativistic impacts in the core region, a double numerical basis set with polarization (DNP) and the DFT semi-core pseudopotential (DSPP) were utilized.[38,39] All the calculations were completed with Grimme dispersion correction (DFT-D2) for van der Waals forces and large interactions.[40] We used the spin-unrestricted method, which employed separate orbitals for spin-up and spin-down electrons, to acquire a more accurate representation of uncoupled electron systems. Furthermore, the Tkatchenko–Scheffler (TS) dispersion correction was utilized to account for interactions produced by van der Waals forces.[41–43] For this study, we used a $3 \times 3 \times 1$ supercell with a 20 Å vacuum layer, containing 34 atoms. Earlier studies confirm that a 3×3 supercell works well for gas adsorption, and a 20 Å vacuum space prevents interactions between neighboring units.[44,45] All calculations were performed using an established *k*-point grid of $4 \times 4 \times 1$ and an entire cut-off radius of 5.4 Å. In an optimization process, the maximum force, displacement convergence, and energy tolerance are 0.002 Ha Å^{-1}, 0.005 Å, and 1×10^{-5} Ha, respectively.[46,47]

The cohesive energy of our proposed nanosheets was calculated using the following equation to investigate their structural stability.[46]

$$E_{\mathrm{coh}} = \frac{E_{\mathrm{MXene}} - AE_{\mathrm{TM}} - BE_{\mathrm{X}}}{A + B} \quad (1)$$

where, E_{TM} and E_{X} represent the energies of the transition metal atoms (Zr or Hf) and the non-metal atoms (N or C),

Table 1 Comparison of gas sensing materials based on MXenes

Author	Sensing materials	Targeted gases	Methods	Key findings	Ref.
J. Liang *et al.*	MXene-based biosensor	Biomolecules	DFT	Good biocompatibility; potential piezoresistive biosensor.	24
Q. Zhou *et al.*	Ni-doped Zr_2CO_2/MoS_2	HCN	DFT	Enhanced adsorption/sensing *via* O-vacancies and doping.	25
R. K. Choudhury	W_2CT_2 (T = O, F)	NH_3	DFT	Strong physisorption, charge transfer, and conductivity.	26
Z. Li *et al.*	$Ti_3C_2O_2$	NH_3, H_2S, CO_2	DFT	Strong adsorption; excellent sensitivity to toxic gases.	27
R. P. Reji *et al.*	Sc_2CO_2	VOC_S (ethanol, acetonitrile, 2-propanol)	DFT	Dual-mode sensing; high sensitivity, fast recovery.	28
J. Su *et al.*	Zn–Co doped $Ti_3C_2O_2$	NO	DFT	Enhanced NO adsorption; improved sensitivity.	29
K. Boonpalit *et al.*	$Sc@Zr_3C_2O_2$, $Y@Zr_3C_2O_2$	CO	DFT	Good sensitivity, stability, and fast recovery.	30
Xi. Li *et al.*	$Zr_3C_2O_2$	Multiple gases	DFT	Gas sensing tunable *via* surface groups and strain.	31

respectively. The variables A and B indicate the number of transition metal and non-metal atoms, respectively.

The adsorption energy was obtained to explore the ability of gas molecules and nanosheets to adsorb,[48]

$$E_{ads} = E_{nanosheet+gas} - E_{nanosheet} - E_{gas} \quad (2)$$

where $E_{nanosheet+gas}$ is the total energy of the nanosheets with the absorbed gas molecules; $E_{nanosheets}$ and E_{gas} are the energy of the nanosheets and the energy of the gas molecules before adsorption, respectively.

Through Mulliken and Hirshfeld's charge evaluation, the total charge transfer (Q_t) between the gas molecules and the nanosheets was studied. Q_t was determined by,[49]

$$Q_t = Q_{ads\text{-}gas} - Q_{iso\text{-}gas} \quad (3)$$

In this case, $Q_{ads\text{-}gas}$ denotes the net charge of the gas molecules following adsorption, while $Q_{iso\text{-}gas}$ denotes the net charge of the isolated gas molecules. The CASTEP module was employed to generate the charge density difference (CDD) maps with a cutoff energy of 400 eV and a k-point grid of $3 \times 3 \times 1$ to enable determination of the charge transfer behavior,[47]

$$\Delta\rho = \rho_{nanosheet+gas} - \rho_{nanosheet} - \rho_{gas} \quad (4)$$

In this case, $\rho_{nanosheet+gas}$, $\rho_{nanosheet}$ and ρ_{gas} are the charge density of the nanosheets with the absorbed gas molecules, nanosheets and gas molecules, respectively.

3. Results and discussion

3.1 Geometry and structural stability

In this investigation, four $3 \times 3 \times 1$ supercells of carbide and nitride MXenes (Hf_2C, Hf_2N, Zr_2C, and Zr_2N) and their Janus MXenes (ZrHfC and ZrHfN) were chosen. The Janus MXenes were created by replacing one Zr/Hf layer of any of the initial four nanosheets (Hf_2C/N or Zr_2C/N) with Hf/Zr, forming ZrHfC and ZrHfN. Each of these nanosheets has 27 atoms. Hf_2N, Zr_2N, and ZrHfN contain 9 N atoms each, and the same goes for Hf_2C, Zr_2C, and ZrHfC, but here they have 9 C atoms each. In both the Hf_2N and Hf_2C structures, 18 Hf atoms are present, and 18 Zr atoms are present in both the Zr_2N and Zr_2C structures. Additionally, 9 N or C atoms, along with 9 Hf and Zr atoms, respectively, are present in the ZrHfN and ZrHfC structures. The N–Hf bond length and bond angle of Hf–N–Hf in the optimized Hf_2N structure are determined to be 2.204 Å and 87.150°, respectively, consistent with previous findings.[50] For Hf_2C, the C–Hf bond length and bond angle of Hf–C–Hf are determined to be 2.204 Å and 87.150°, respectively, and are comparable to the prior value.[51] Additionally, the obtained value is the same in the instances of Zr_2N and Zr_2C. The ZrHfC monolayer, as seen in Fig. 1, is made up of three distinct atom layers: Hf, Zr, and N. The C layer is located in the center of the Hf and Zr layers. In the same way, the ZrHfN monolayer is composed of three layers, with the N layer remaining in the midst of the Hf and Zr layers. The ZrHfC and ZrHfN heterolayer structures show the maximum stability and lowest

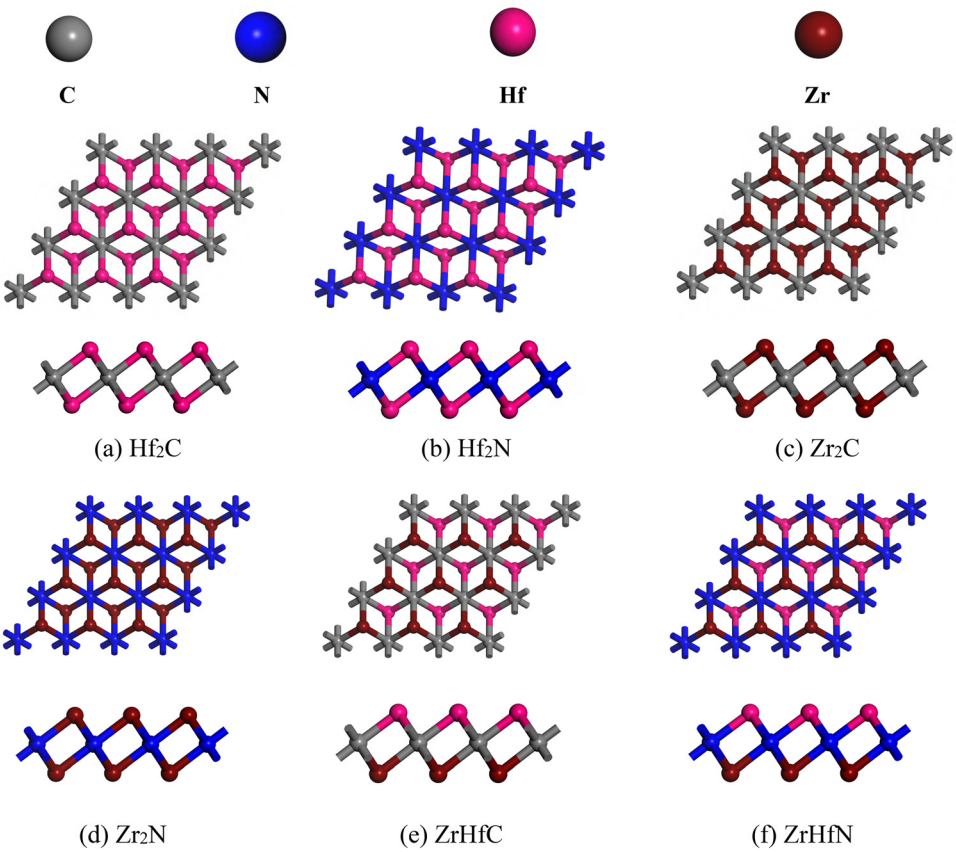

Fig. 1 Top and side views of the optimized structures of the nanosheets.

formation energies of all the mixed phases. The Hf–C and Zr–C bond lengths in the ZrHfC structure are optimized to be 2.192 Å and 2.218 Å, respectively, and the Hf–N–Zr bond angle is calculated to be 92.909°. For ZrHfN, the optimized Hf–N–Hf bond angle is 46.128°, and the Hf–N bond length is 2.192 Å, both in useful agreement with previously revealed findings.[50] It is shown in Fig. 2–5 that no structural deformation occurs in these nanosheets after optimization. Therefore, the stability of the structure remains unchanged in this gas sensor. In this investigation, we also relaxed four hazardous gases, namely CO, NO, NO_2, and SO_2, in the ground state. The optimized structures of these gas molecules are shown in Fig. 1. In CO and NO, the C–O and N–O bonds have lengths of 1.145 Å and 1.166 Å, respectively. The N–O bond length in the NO_2 molecule is 1.213 Å, while the S–O bond length in the SO_2 molecule is 1.464 Å. NO_2 and SO_2 have V-shaped structures, with calculated O–N–O and O–S–O bond angles of 133.271° and 119.712°, respectively.

We calculated the cohesive energy using eqn (1) to understand the bond strength in the crystal structures—the more negative the cohesive energy, the more stable the structure. The cohesive energies are −6.96, −6.59, −6.97, −6.61, −6.98, and −6.62 eV for Hf_2C, Hf_2N, Zr_2C, Zr_2N, ZrHfC, and ZrHfN, respectively, which is consistent with previous findings.[50] In our findings, the cohesive energy is larger (more negative) in the carbide MXene than that of nitride ones, which was also found by Shein *et al.*[52] The cohesive energies increase in this order: Hf_2N < Zr_2N < ZrHfN < Hf_2C < Zr_2C < ZrHfC, which shows that ZrHfC is the most stable among the nanosheets.

3.2 Adsorption behavior of Hf_2C and Hf_2N towards the CO, NO, NO_2, and SO_2

The adsorption properties of CO, NO, NO_2, and SO_2 on the Hf_2C and Hf_2N nanosheets were evaluated by analyzing the adsorption energy (E_{ads}), minimum adsorption distance (d_{min}), and charge transfer (Q_t). The calculated values are summarized in Table 2, and the corresponding optimized structures are illustrated in Fig. 2. When the adsorption process is positive, it indicates an endothermic reaction; conversely, the negative adsorption value indicates an exothermic reaction and also illustrates the attractive connection between gas molecules and nanosheets.[53] Here, the significant values of E_{ads} are −2.32, −4.42, −7.63, and −9.61 eV for CO, NO, NO_2, and SO_2 gas molecule adsorption on the Hf_2C nanosheet at a distance of about 2.155, 2.102, 2.085, and 2.048 Å, respectively. Similarly, in the case of the Hf_2N nanosheet, the values of E_{ads} are −1.65, −4.82, −7.38, and −11.52 eV for CO, NO, NO_2, and SO_2 gas molecules at a distance of 2.354, 2.054, 2.040, and 2.034 Å, respectively. Based on the study findings by Yong *et al.*, the highest E_{ads} values for CO, NO, NO_2, and SO_2 on the C_2N monolayer are −0.239 eV, −0.471 eV, −1.665 eV, and −1.304 eV, respectively.[54] Aghaei *et al.* observed that the adsorption energies of toxic gas molecules (NO, CO, and NO_2) on graphene-like boron carbide (BC_3) were −1.11 eV, −1.34 eV, and −1.13 eV, respectively.[55] Q. Hu *et al.* demonstrated $Hf_3C_2O_2$ MXene's gas sensing potential through its moderate adsorption energies of −0.197 eV (CO) and −0.174 eV (NO).[56] According to Salih *et al.*, gold (Au) and silver (Ag) co-doped molybdenum disulfide (Au–Ag–MoS_2) demonstrated promising NO and NO_2 gas sensing capabilities, with adsorption energies of −0.553 eV and −2.603 eV, respectively.[56] Based on the current comprehensive study, the E_{ads} energy for the Hf_2C and Hf_2N nanosheets is better than the previous ones, confirming the superior sensing potential of Hf-based MXenes compared with many other 2D materials.

For both Hf_2C and Hf_2N nanosheets, the E_{ads} increases in the order CO < NO < NO_2 < SO_2, while d_{min} follows the

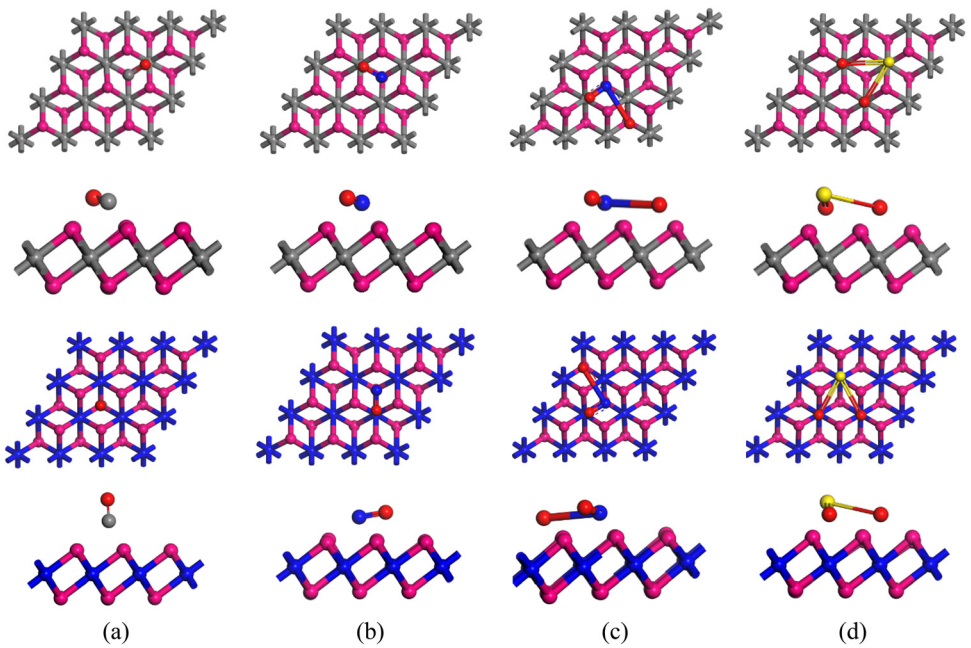

Fig. 2 Top and side views of (a) CO, (b) NO, (c) NO_2, and (d) SO_2 adsorbed on the Hf_2C (top two rows) and Hf_2N (bottom two rows) nanosheets.

Table 2 Calculated values of the adsorption energy (E_{ads}), minimum adsorption distance (d_{min}), and charge transfer between the gas molecules and the Hf_2C, Hf_2N, Zr_2C and Zr_2N nanosheets

Nanosheets	Gas molecules	E_{ads} (eV)	d_{min} (Å)	Q_t (e) (Mulliken)	Q_t (e) (Hirshfeld)
Hf_2C	CO	−2.32	2.155	−0.200	−0.162
	NO	−4.42	2.102	−0.432	−0.288
	NO_2	−7.63	2.085	−1.906	−0.673
	SO_2	−9.61	2.048	−1.964	−0.822
Hf_2N	CO	−1.65	2.354	−0.109	−0.214
	NO	−4.82	2.054	−0.359	−0.276
	NO_2	−7.38	2.04	−0.522	−0.437
	SO_2	−11.52	2.034	−0.327	−0.228
Zr_2C	CO	−2.84	2.176	−0.913	−0.333
	NO	−4.97	2.136	−1.030	−0.349
	NO_2	−9.27	2.108	−1.871	−0.657
	SO_2	−10.60	2.063	−1.959	−0.812
Zr_2N	CO	−3.37	2.139	−0.152	−0.107
	NO	−5.13	2.154	−0.477	−0.29
	NO_2	−9.87	2.165	−0.44	−0.331
	SO_2	−6.56	2.099	−0.329	−0.276

reverse trend. Furthermore, all of the E_{ads} values are observed to be negative, indicating an exothermic reaction. NO_2 and SO_2 molecules show a stronger interaction with Hf_2C and Hf_2N nanosheets than CO and NO molecules, which are also adsorbed on the surfaces of Hf_2C and Hf_2N in chemisorption. However, when the adsorption energy is too high, the desorption process slows, *i.e.*, the recovery time increases, which is unsuitable for a good conductor. This indicates that these two nanosheets show better performance as a gas sensor material for detecting CO and NO rather than NO_2 and SO_2.

Mulliken and Hirshfeld charge analysis also indicates that Hf_2C and gas molecules interact strongly by sharing a vast amount of charge (Mulliken) $-0.200e$ (CO), $-0.432e$ (NO), $-1.906e$ (NO_2) and $-1.964e$ (SO_2), where Hf_2C plays the role of electron donor and toxic gas molecules are used as electron acceptors. Charge transfer analysis reveals that the Hf_2C nanosheets exhibit a slightly greater charge transfer with gas molecules than Hf_2N. However, a significant amount of electron transfer occurs in Hf_2N. The Hirshfeld charge of $0.214e$ and Mulliken charge of $0.359e$, $0.522e$, and $0.327e$ are transferred to the gas molecules CO, NO, NO_2, and SO_2, respectively. The Q_t values for CO, NO, NO_2, and SO_2 adsorption indicate that Hf_2N serves as an electron donor. Thus, for Hf_2C, the charge transfer follows the order: CO < NO < NO_2 < SO_2, while for Hf_2N, the trend is CO < SO_2 < NO < NO_2. Previously, Yong *et al.* reported charge transfers of $0.031e$, $0.294e$, $-0.017e$, and $-0.088e$ between C_2N and CO, NO, NO_2, and SO_2 gas molecules, respectively.[54] According to S. M. Aghaei *et al.*, charge transfers occur between BC_3 and gas molecules as follows: $0.09e$ from BC_3 to CO, $0.65e$ from NO to BC_3, and $0.48e$ from NO_2 to BC_3.[55] E. Salih *et al.* demonstrated significant charge transfer from NO ($0.220e$) and NO_2 ($0.448e$) to the Au–Ag–MoS_2.[57] Our results, in particular, exhibit higher charge transfer values, proving that the material according to this study interacts with these gas molecules more strongly, which implies it has promising potential for gas-sensing purposes.

3.3 Adsorption behavior of Zr_2C and Zr_2N towards the CO, NO, NO_2, and SO_2

To measure the adsorption capacity of the aforementioned gas molecules on other nanosheets, specifically Zr_2C and Zr_2N, we calculated the adsorption energy with adsorption distance and net charge transfer using eqn (2) and (3), which are listed in Table 1, and Fig. 3 depict the top and side views of the following gas molecule adsorption on the Zr_2N and Zr_2C nanosheets.

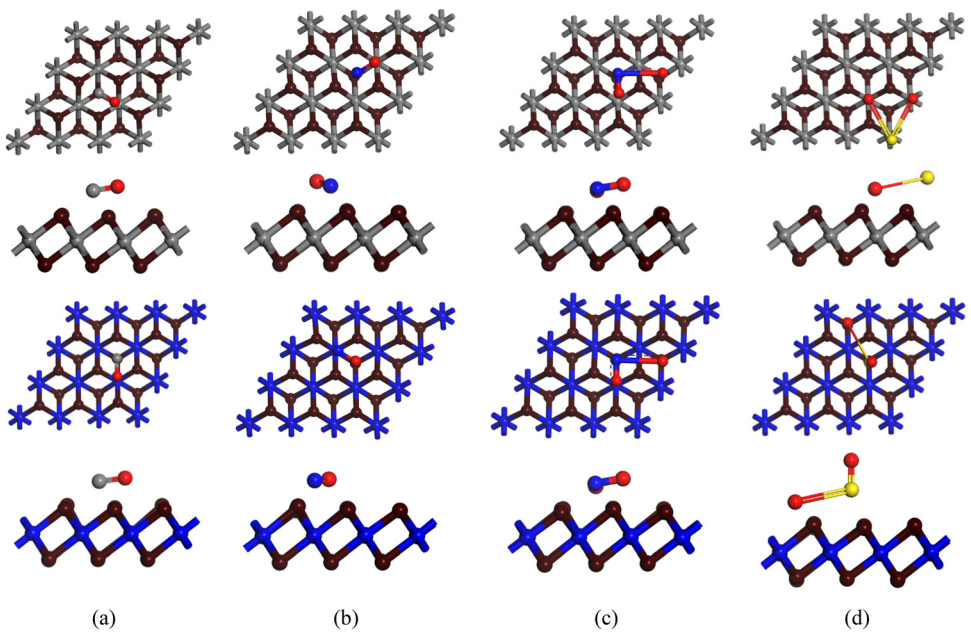

Fig. 3 Top and side views of (a) CO, (b) NO, (c) NO_2, and (d) SO_2 adsorbed on the Zr_2C (top two rows) and Zr_2N (bottom two rows) nanosheets.

The various adsorption sites on the nanosheets and gas molecules' orientations were investigated to find the most stable complex. The significant values of E_{ads} are −2.84, −4.97, −9.27, and −10.60 eV, respectively, for CO, NO, NO_2, and SO_2 gas molecule adsorption on Zr_2C nanosheets from distances of 2.176, 2.136, 2.108, and 2.063 Å, respectively. Again, the values of E_{ads} are −3.37, −5.13, −9.87, and −6.56 eV for CO, NO, NO_2, and SO_2 gas molecule adsorption on Zr_2N nanosheets at a distance of 2.139, 2.154, 2.165, and 2.099 Å, respectively. According to H. Y. Ammar *et al.*, the E_{ads} values of CO and NO are significantly enhanced when the $B_{12}N_{12}$ nanocage is doped with transition metals (Mn and Fe). Specifically, $MnB_{11}N_{12}$ exhibits adsorption energies of −0.510 eV (CO) and −0.740 eV (NO), while $FeB_{11}N_{12}$ shows higher adsorption energies of −0.760 eV (CO) and −1.013 eV (NO).[58] Y. Wu *et al.* calculated adsorption energies on B-doped graphdiyne (B-GDY), showing weak CO interaction (−0.068 eV), moderate SO_2 adsorption (−0.173 eV), and stronger NO_x capture (−0.458 eV for NO, −0.541 eV for NO_2).[59] J. Ren *et al.* demonstrated that pristine hexagonal boron arsenide (BAs) exhibits distinct gas adsorption capabilities, with calculated adsorption energies of −0.27 eV for CO, −0.18 eV for NO, −0.43 eV for NO_2, and a significantly stronger −0.92 eV for SO_2.[60] Our study shows that Zr_2C and Zr_2N nanosheets have stronger adsorption energy than the previous findings. Numerically, the adsorption energy trend upon adsorption on Zr_2C is CO < NO < NO_2 < SO_2, while for Zr_2N it follows CO < NO < SO_2 < NO_2. From the above observation, we have seen that the maximum adsorption occurs for SO_2 in the case of Zr_2C nanosheets, and for Zr_2N nanosheets, it occurs for NO_2 gas molecules. Also, the adsorption energy for CO and NO for both of these nanosheets is in the chemisorption range.

Mulliken charge analysis also shows that a considerable amount of charge is transferred to the nanosheets, indicating a strong interaction between the gas molecules and these two nanosheets. In terms of Zr_2C, the charge transfer increases in the order: CO (−0.913*e*) < NO (−1.030*e*) < NO_2 (−1.871*e*) < SO_2 (−1.959*e*), while for Zr_2N the trend follows CO (−0.152*e*) < SO_2 (−0.329*e*) < NO_2 (−0.440*e*) < NO (−0.477*e*). H. Y. Ammar *et al.* found that CO transferred 0.222*e* to $MnB_{11}N_{12}$ and 0.269*e* to $FeB_{11}N_{12}$, while NO received 0.045*e* from $MnB_{11}N_{12}$ and transferred 0.053*e* to $FeB_{11}N_{12}$.[58] Y. Wu *et al.* reported charge sharing between the B-GDY supercell and gas molecules, with values of −0.008*e* (CO), 0.083*e* (NO), −0.563*e* (NO_2), and −0.071*e* (SO_2).[59] J. Ren *et al.* reported minimal charge transfer between monolayer BAs and CO/NO molecules, while stronger interactions were observed with NO_2 (−0.231*e*) and SO_2 (−0.179*e*).[60]

From this table (Table 2), the atomic-level characteristics of the gases and the MXene surfaces can be used to explain the adsorption energies and charge transfer trends seen for distinct gas molecules on different MXenes. Because of their high electronegativity and polarity, which enable them to draw more electrons from the MXene surface, SO_2 and NO_2 exhibit the strongest adsorption and largest charge transfer. CO, on the other hand, has the smallest charge transfer and the weakest adsorption because of its smaller size and lower electronegativity. Furthermore, compared to carbides, nitride-based

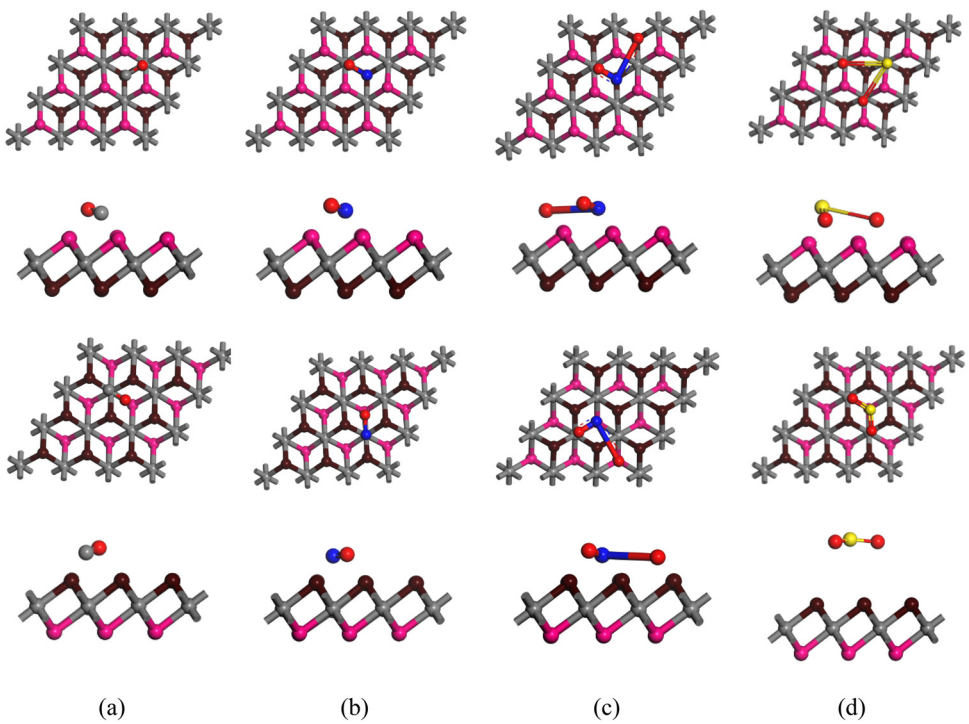

Fig. 4 Top and side views of (a) CO, (b) NO, (c) NO_2, and (d) SO_2 adsorbed on the ZrHfC, where the top two rows are Hf sites and the bottom two rows are Zr sites of the nanosheets.

MXenes (Hf_2N, Zr_2N) frequently exhibit slightly greater adsorption because nitrogen atoms offer more active sites for electron transfer, improving the interaction with polar gas molecules.

3.4 Adsorption behavior of ZrHfC and ZrHfN towards the CO, NO, NO_2, and SO_2

To get more insight into the adsorption phenomena of Janus carbide and nitride MXene, we similarly observed the adsorption behavior of ZrHfC and ZrHfN towards the gas molecules. Fig. 4 and 5 show the top and side views after gas molecule adsorption on the ZrHfC and ZrHfN nanosheets. To better investigate the adsorption behavior, gas molecules are adsorbed on the Zr and Hf sites of the nanosheets. The significant values of E_{ads} at the Zr sites are −2.77, −4.98, −9.17, and −0.40 eV, respectively, for CO, NO, NO_2, and SO_2 gas molecule adsorption on the ZrHfC nanosheets at a distance of 2.455, 2.097, 2.092, and 2.046 Å, respectively (Table 3). The significant values of E_{ads} at the Hf sites are −0.29, −4.57, −9.50, and −10.68 eV, respectively, for CO, NO, NO_2, and SO_2 gas molecule adsorption on the ZrHfC nanosheets at a distance of 2.134, 2.183, 2.135, and 2.046 Å, respectively. Numerically, the absolute values of adsorption energy for the Zr sites are SO_2 < CO < NO < NO_2, and for the Hf sites are CO < NO < NO_2 < SO_2. In these nanosheets, the Zr site for CO and the Hf site for SO_2 are substantially more reactive. Comparing the above two adsorption sites, we observe that the maximum adsorption occurs at NO_2 gas molecules, which is −9.17 eV for Zr sites, and for the Hf sites, it occurs for SO_2 (−10.68 eV) gas molecules. The most favorable adsorption sites are found at distances of 2.115 Å, 2.051 Å, 2.039 Å, and 1.098 Å on the Zr site of ZrHfN, with adsorption energies of approximately −3.30 eV, −4.78 eV, −10.13 eV, and −6.54 eV for CO, NO, NO_2, and SO_2, respectively.

Table 3 Calculated values of the adsorption energy (E_{ads}), minimum adsorption distance (d_{min}), and charge transfer between the gas molecules and the ZrHfC and ZrHfN nanosheets

Nanosheets	Gas molecules	Sites	E_{ads} (eV)	d_{min} (Å)	Q_t (e) (Mulliken)	Q_t (e) (Hirshfeld)
ZrHfC	CO	Zr	−2.77	2.455	−0.915	−0.364
		Hf	−0.29	2.134	−0.027	−0.038
	NO	Zr	−4.98	2.097	−0.172	−0.124
		Hf	−4.57	2.183	−1.033	−0.367
	NO_2	Zr	−9.17	2.092	−1.88	−0.656
		Hf	−9.50	2.135	−1.887	−0.677
	SO_2	Zr	−0.40	2.046	−0.245	−0.252
		Hf	−10.68	2.046	−1.945	−0.830
ZrHfN	CO	Zr	−3.30	2.115	−1.00	−0.384
		Hf	−2.76	2.167	−0.955	−0.340
	NO	Zr	−4.78	2.051	−0.701	−0.349
		Hf	−5.32	2.146	−1.038	−0.358
	NO_2	Zr	−10.13	2.039	−1.908	−0.667
		Hf	−10.14	2.039	−2.585	−1.018
	SO_2	Zr	−6.54	1.098	−0.053	−0.504
		Hf	−11.55	2.038	−1.923	−0.805

According to Table 3, SO_2 and NO_2 show the greatest amount of adsorption and strongest charge transfer on both ZrHfC and ZrHfN due to their high electronegativity and polarity, while CO exhibits the weakest because of its tiny dimensions and low electronegativity. Since nitrogen provides more active sites for electron transfer, nitride-based MXenes (ZrHfN) generally adsorb gases more strongly than carbides (ZrHfC).

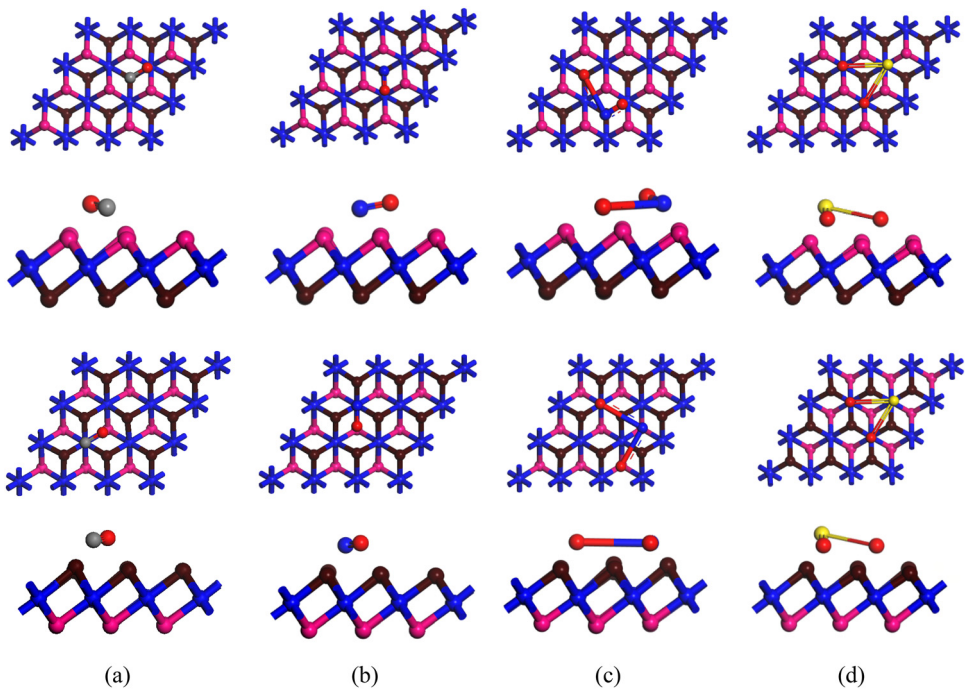

Fig. 5 Top and side views of (a) CO, (b) NO, (c) NO_2, and (d) SO_2 adsorbed on the ZrHfN, where the top two rows are Hf sites and the bottom two rows are Zr sites of the nanosheets.

Similarly, for the Hf site, CO, NO, NO_2, and SO_2 molecules adsorb on ZrHfN at minimum distances of 2.167 Å, 2.146 Å, 2.039 Å, and 2.026 Å, with corresponding adsorption energies of about −2.76 eV, −5.32 eV, −10.14 eV, and −11.52 eV, respectively. The adsorption energies on the Zr site follow the trend: CO < NO < SO_2 < NO_2, and on the Hf site, that is, CO < NO < NO_2 < SO_2. The adsorption energies indicate that all four gases interact with both ZrHfC and ZrHfN through chemisorption, with substantially larger values for NO_2 and SO_2 gas molecules. Previous study by Kharb *et al.* demonstrates that O-functionalized TiVC MXene exhibits exceptional gas adsorption capabilities, with energies of −0.88 eV (CO), −0.72 eV (NO), −1.06 eV (NO_2), and −0.28 eV (SO_2).[61] The highest adsorption energy was found on Pt-decorated Hf_2CO_2, with values of −3.45 eV for CO as reported by Boonpalit *et al.*[30] Hu *et al.* reported adsorption energies of 2.07 eV for CO, 3.05 eV for NO, and 2.53 eV for NO_2 on Cr–C_9N_4, while for Fe_2–C_9N_4, the E_{ads} values were 2.60 eV for CO, 3.07 eV for NO, and 2.45 eV for NO_2.[62] Compared to these earlier findings, our nanosheets demonstrate stronger adsorption.

We also noticed that the electron transfer between the gases and the heterostructures is significantly larger on both sites of the nanosheets when considering Mulliken and Hirshfeld charge analysis. The Mulliken charge transfer from ZrHfC to gas molecules is significant, with approximately 0.915*e* for CO, 0.172*e* for NO, 1.88*e* for NO_2, and 0.245*e* for SO_2 at the Zr site during the interaction between the nanosheets and gas molecules. The charge transfers of 0.027*e*, 1.033*e*, 1.887*e*, and 1.945*e* at the Hf site from ZrHfC to CO, NO, NO_2, and SO_2 gas molecules, respectively. For ZrHfN, a notable amount of charge is transferred from the nanosheets to the toxic gases. At the Zr site, Mulliken charges of 1.00*e*, 0.701*e*, 1.908*e*, and 0.504*e* (Hirshfeld) are transferred to CO, NO, NO_2, and SO_2, respectively. Meanwhile, at the Hf site, the Mulliken charge transferred to CO, NO, NO_2, and SO_2 has values of 0.955*e*, 1.038*e*, 2.585*e*, and 1.93*e*, respectively. K. Ma *et al.* reported charge transfers of −0.98*e* (CO–Zr–stanene), −1.293*e* (NO–Nb–stanene), −0.63*e* (NO_2–Zr–stanene), and −0.67*e* (SO_2–Nb–stanene).[63] Z. Wu *et al.* found charge transfers of 0.108*e* (CO), 0.306*e* (NO), 0.513*e* (NO_2), and 0.589*e* (SO_2) for adsorption on Al-doped Ti_2CO_2 nanosheets.[64] Mushtaq *et al.* observed the highest charge transfers: −2.52*e* (NO on a hollow site) and −3.59*e* (NO_2 on a Si-atom site), with negative values indicating electron donation from the CFMS (001) surface to NO_x.[65] Compared to previous studies, our proposed heterostructure demonstrates significantly higher charge transfer values.

3.5 Electronic properties

To better understand the performance of these MXene nanosheets, the electronic characteristics of all six nanosheets have been examined. We checked their band structures, density of states (DOS) spectra, and charge density difference (CDD) maps. The electronic band structures were computed along a high-symmetry path through the Brillouin zone: starting at *Γ* (0,0,0), then to *F* (0,0.5,0), next to *K* (−0.333,0.667,0), and back to *Γ* (0,0,0) (Fig. 6). In all cases, the results clearly indicate that several bands cross the Fermi level, confirming the metallic character of the system, which matches with previous findings.[50] The absence of a band gap ensures a continuous

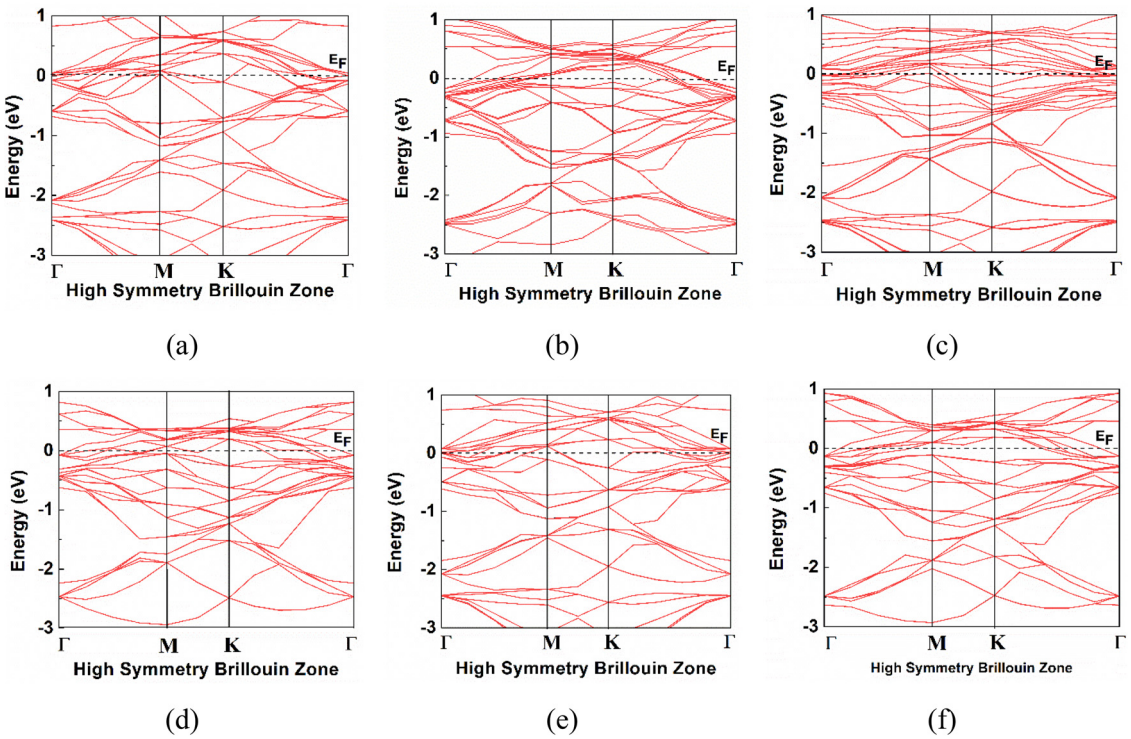

Fig. 6 The band structures of the nanosheets (a) Hf_2C, (b) Hf_2N, (c) Zr_2C, (d) Zr_2N, (e) ZrHfC, and (f) ZrHfN.

distribution of electronic states at the Fermi level, which is favorable for fast electron transport. In addition, the presence of steeply dispersive bands near the Fermi level suggests low effective mass and high carrier mobility. The DOS plots represent the distribution of electronic states at different energy levels. To investigate how gas adsorption affects the electronic properties of the nanosheets, we analyzed both the total density of states (TDOS) and partial density of states (PDOS), as illustrated in Fig. 7. After adsorption of the CO and NO gases on the nanosheets, no significant DOS peak was found at the Fermi level, but minor changes were found near the Fermi level after the adsorption of NO_2 and SO_2 gas molecules. From the DOS spectra, it also confirmed that all the optimized complexes exhibited metallic behavior due to the non-zero DOS at the Fermi level (E_F). From the plots, it is evident that there is significant overlap between the orbitals of the gas molecules and the MXene surface atoms, particularly near the Fermi level. This orbital hybridization indicates strong electronic interactions between the gas molecules and MXenes, confirming the chemisorption mechanism. The intensity and position of the peaks also suggest that Hf- and Zr-based MXenes interact more strongly with NO and NO_2 compared to CO and SO_2, consistent with the adsorption energy and charge transfer results.

We also studied the charge density difference (CDD) maps to examine charge redistribution, bonding interactions, and electric charge transfer behavior. The CDD maps in Fig. 8 illustrate the charge transfer process, where cyan and yellow colors indicate regions of charge loss and gain, respectively. For clearer visualization, the iso-surface value was set to $0.03e$ $Å^{-3}$ to effectively represent charge density distributions. The CDD map clearly shows electron redistribution throughout the system by highlighting these regions. From Fig. 8, the transfer of a significant amount of charges between the gas molecules (CO) and the nanosheets is clearly observed. From the Mulliken charge analysis, we observe electron transfers of $0.200e$ (for CO) to Hf_2C, $0.109e$ to Hf_2N, $0.913e$ to Zr_2C, $0.152e$ to Zr_2N, $0.915e$ to ZrHfC, and $1.000e$ to ZrHfN. Charge transfer took place between the gas molecules and the adjacent atoms on the nanosheet surface.

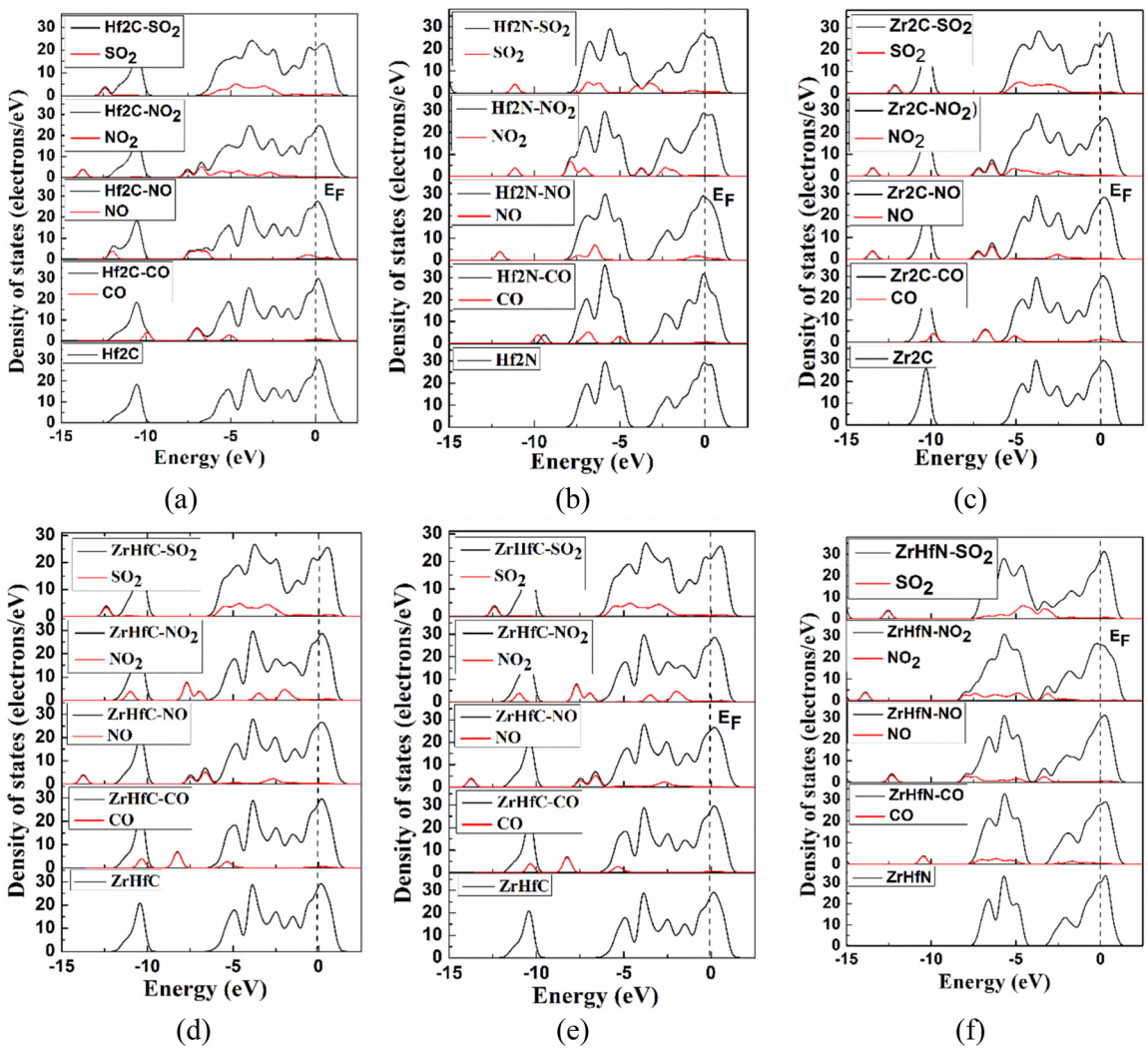

Fig. 7 The total and partial DOS for (a) Hf_2C, (b) Hf_2N, (c) Zr_2C, (d) Zr_2N, (e) ZrHfC, and (f) ZrHfN nanosheets before and after adsorption of CO, NO, NO_2, and SO_2 gas molecules.

3.6 Recovery time

In nanosheets, the recovery time (τ) is the time needed for gas molecules to desorb from the surface. Higher performance and accurate repeated use require faster sensor renewal, which is indicated by a shorter recovery time. An increase in adsorption energy leads to the recovery time τ being boosted exponentially, and standard transition state theory may clarify this fact as:[66]

$$\tau = \frac{1}{\vartheta_0} e^{\left(\frac{-E_{ads.}}{k_B T}\right)} \quad (5)$$

where ϑ_0 denotes the attempt frequency, Boltzmann's constant is represented as k_B, and T is the absolute temperature in Kelvin. According to the equation, a longer recovery time occurs with a higher adsorption energy. While our proposed nanosheets have significantly higher adsorption energy, this also creates a drawback, like gas molecules taking much longer to desorb. The experiment's results revealed that exposure to vacuum UV light at various frequencies (10^{12} s^{-1}, 3×10^{14} s^{-1}, and 10^{18} s^{-1}) and at varying temperatures (300 K, 400 K, and 500 K) was suitable for recovering the detector.[54,55,66] In our observations, all the nanosheets exhibit stronger adsorption of gases, leading to significantly longer recovery times. The adsorption energy for SO_2 and NO_2 is much higher compared to that for CO and NO across all nanosheets. As a result, molecular desorption from the surface is hindered, resulting in a slower recovery process. For CO adsorption (E_{ads} = 1.65 eV) on Hf_2N nanosheets, the recovery time is predicted to be 2.34 minutes at 500 K, along with a frequency of 3×10^{14} s^{-1}. Since the absorption energies are greater in all instances, the recovery time is considerably longer. At a frequency of 10^{18} s^{-1} and a temperature of 500 K, the recovery time for NO on Hf_2N is 3.249×10^{31} s. For Hf_2C, the recovery times are 2.98×10^5 s for CO and 3.45×10^{62} s for NO. In the case of Zr_2C, the recovery times are 4.141×10^{10} s (CO) and 1.202×10^{32} s (NO), whereas for Zr_2N, they are 9.07×10^5 s (CO) and 4.92×10^{33} s (NO), respectively. For the heterostructures at the Zr site, ZrHfC exhibits recovery times of 8.16×10^9 s (CO) and 1.52×10^{32} s (NO). Similarly, ZrHfN shows recovery times of 1.79×10^{15} s (CO) and 1.46×10^{30} s (NO).

3.7 Sensitivity

It's crucial to examine a material's work function (φ) before using it as a sensing device. Because the work function of material surfaces influences the adsorption energy and charge transfer process, it is important for gas sensing. We studied how gas molecules change the work function of the nanosheets. To account for the interaction of dipoles, particular attention has been paid to the dipole slab correction in the work function calculation.[55] In φ-based sensors, adsorbed gas molecules modify the work function, altering the material's electron emission. This work function shift changes the gate voltage, creating a detectable electrical signal for gas sensing.[67,68] The variation in work function due to gas adsorption was computed by,[47]

$$\Delta\varphi = \frac{\varphi_c - \varphi_n}{\varphi_n} \quad (6)$$

where φ_c is the work function after the absorption of gas molecules, and φ_n is the nanosheets' work function before adsorption. The bar diagram of the φ variation following gas molecule adsorption is displayed in Fig. 9. The results of our investigation showed that the work functions for Hf_2C, Hf_2N, Zr_2C, Zr_2N, ZrHfC, and ZrHfN nanosheets were, respectively, 5.14 eV, 5.13 eV, 5.24 eV, 5.24 eV, 5.19 eV, and 5.18 eV. Following the adsorption of gas molecules, a negative change implies a decrease in work function, whereas a positive change suggests an increase. A major transfer in charge resulted in an increase. During gas adsorption on the nanosheets, the work function increases for all systems except in the following cases: Hf_2C with CO, NO_2, and SO_2; Hf_2N with CO; Zr_2N with NO and SO_2; and ZrHfC with CO.

After the adsorption of CO, NO_2, and SO_2 on Hf_2C, the φ values decreased, with the most significant negative change in φ observed for NO_2 (about 3.11%). For Hf_2N, the greatest positive change in φ was observed for SO_2 (approximately

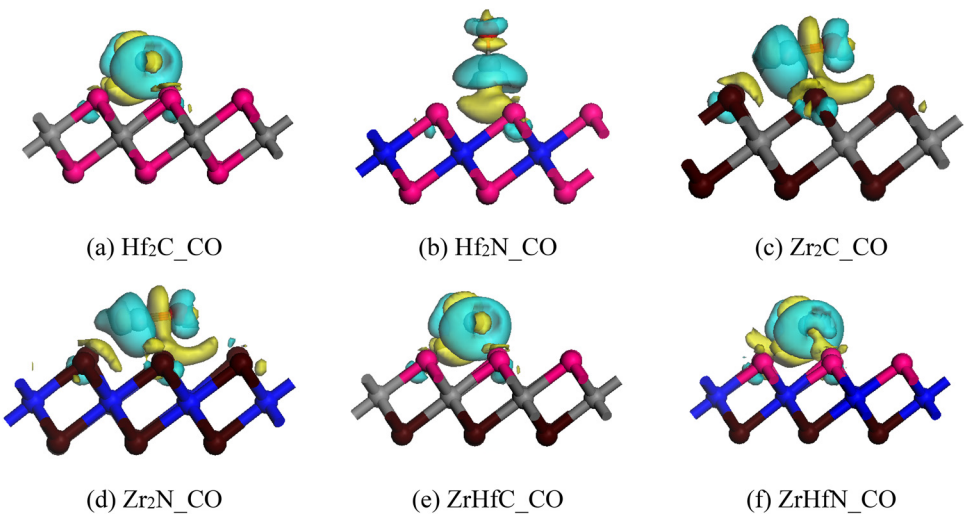

Fig. 8 CDD maps of the CO gas adsorbed nanosheets, where the iso-value was set at $\pm 0.03e$ Å^{-3}.

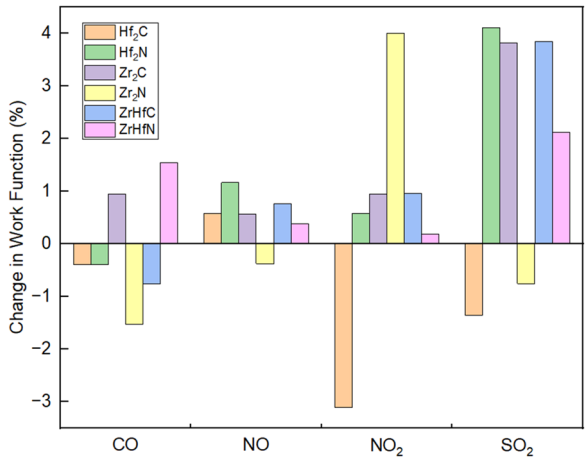

Fig. 9 The variation in the nanosheets' work function after the gas molecules' adsorption.

4.11%) due to a significant Δq of around $0.327e$ from the Hf_2N to SO_2. For Zr_2C, φ experiences minor changes while adsorbing CO, NO, and NO_2 gas molecules, but it significantly rises with SO_2 adsorption (around 3.82%) because of high Δq values of about $1.959e$ from Zr_2C to SO_2. For Zr_2N, the only positive variation in the work function is found for the adsorption of NO_2 of about 4% because there is a large charge transfer of $0.329e$ to SO_2, and for other gas adsorption, it is reduced minimally. For the heterostructures, φ varies significantly for the adsorption of SO_2 at about 3.85% and 2.12% for ZrHfC and ZrHfN, respectively, due to the significant charge transfer of about 1.945 and 1.93, respectively.

4 Conclusions

Many harmful gases are currently present in our environment, which affect not only plants and animals but also human health and our daily lives. These harmful gases must be eliminated or filtered to ensure a healthy existence. MXenes have attracted a great deal of attention for their gas-sensing applications. The adsorption characteristics of Hf_2C, Hf_2N, Zr_2C, Zr_2N, ZrHfC, and ZrHfN nanosheets for CO, NO, NO_2, and SO_2 gas molecule adsorption have been examined in this study by employing the DFT approach. Our four MXenes and their Janus MXenes show stable thermodynamic stability, which was confirmed by the negative values of cohesive energies. All nanosheets show metallic behavior. To comprehend the adsorption behavior, the adsorption energy, charge transfer, work function, and electronic characteristics were investigated. The chemisorption of CO and NO on all nanosheets demonstrated better results, according to the adsorption energy, charge transfer, and electric characteristics. However, the adsorption behavior of NO_2 and SO_2 gas molecules was higher, but the recovery time was comparatively much larger for these two gases. The adsorption energies demonstrate strong CO and NO affinity across all six nanosheets, with values of −2.32 eV (CO) and −4.42 eV (NO) for Hf_2C, −1.65 eV (CO) and −4.82 eV (NO) for Hf_2N, −2.84 eV (CO) and −4.97 eV (NO) for Zr_2C, −3.37 eV (CO) and −5.13 eV (NO) for Zr_2N, −2.77 eV (CO) and −4.98 eV (NO) for ZrHfC at the Zr site, and −3.30 eV (CO) and −4.78 eV (NO) for ZrHfN at the Zr site. A significant amount of charge is shared between the nanosheets and the gas molecules, which are also visualized in the CDD maps. The DOS spectra demonstrate that no additional electronic states are created at the Fermi level for CO and NO adsorption on the nanosheets, but a minor contribution has been found near to the Fermi level in the case of NO_2 and SO_2. Moreover, there is a notable variation in the work functions of the nanosheets when gas molecules are adsorbed. Consequently, every computation suggests that every one of the six nanosheets could be helpful in tracking CO and NO toxic gas molecules.

Conflicts of interest

There are no conflicts to declare.

Data availability

The data supporting this article have been included in the manuscript.

Acknowledgements

We thankfully acknowledge the Bangladesh Research and Education Network (BdREN) for their computational access.

References

1 D. E. Schraufnagel, J. R. Balmes, C. T. Cowl, S. De Matteis, S.-H. Jung, K. Mortimer, R. Perez-Padilla, M. B. Rice, H. Riojas-Rodriguez and A. Sood, *Chest*, 2019, **155**, 417–426.
2 M. S. Mian, M. S. Rahman, J. Islam, K. N. Sakib, M. M. Tasnim and S. Yeasmin, *J. Sci. Res.*, 2019, **11**, 263–272.
3 L. D. Rosenthal, *Am. J. Nurs.*, 2006, **106**, 40–46.
4 K. Ueda, *Overcoming Environmental Risks to Achieve Sustainable Development Goals: Lessons from the Japanese Experience*, Springer, 2021, pp. 39–46.
5 O. Badr and S. D. Probert, *Appl. Energy*, 1993, **46**, 1–67.
6 L.-T. Le, K.-B. V. Quang, T.-V. Vo, T.-M. T. Nguyen, T.-V.-H. Dao and X.-T. Bui, *Vietnam J. Sci. Technol. Eng.*, 2024, **66**, 120–128.
7 N. Baig, *Composites, Part A*, 2023, **165**, 107362.
8 M. Kiani, M. U. Rehman, X. Tian and B. Yakobson, *Adv. Mater. Technol.*, 2022, **7**, 2101252.
9 X. Liu, T. Ma, N. Pinna and J. Zhang, *Adv. Funct. Mater.*, 2017, **27**, 1702168.
10 A. VahidMohammadi, J. Rosen and Y. Gogotsi, *Science*, 2021, **372**, eabf1581.
11 S. Alwarappan, N. Nesakumar, D. Sun, T. Y. Hu and C.-Z. Li, *Biosens. Bioelectron.*, 2022, **205**, 113943.
12 M. Ozkan, *MRS Energy Sustain.*, 2024, **11**, 181–190.

13 M. Naguib, V. N. Mochalin, M. W. Barsoum and Y. Gogotsi, *Adv. Mater.*, 2014, **26**, 992–1005.
14 J.-F. Zhang, H.-Y. Cao and H.-B. Wang, *J. Inorg. Mater.*, 2017, **32**, 561–570.
15 S. Gasso, R. Saini, R. Kaur, N. Joshi, S. Sharma and P. Devi, *Mxene-Based Hybrid Nano-Architectures for Environmental Remediation and Sensor Applications*, Elsevier, 2024, pp. 305–326.
16 M. Malaki, X. Jiang, H. Wang, R. Podila, H. Zhang, P. Samori and R. S. Varma, *Chem. Eng. J.*, 2023, **463**, 142351.
17 J. Zhu, E. Ha, G. Zhao, Y. Zhou, D. Huang, G. Yue, L. Hu, N. Sun, Y. Wang and L. Y. S. Lee, *Coord. Chem. Rev.*, 2017, **352**, 306–327.
18 N. García-Romeral, Á. Morales-García, F. Viñes, I. de, P. R. Moreira and F. Illas, *Phys. Chem. Chem. Phys.*, 2023, **25**, 31153–31164.
19 S. Kumar, N. Kumari and Y. Seo, *J. Energy Chem.*, 2024, **90**, 253–293.
20 J. Bjork and J. Rosen, *Chem. Mater.*, 2021, **33**, 9108–9118.
21 P. Srivastava, A. Mishra, H. Mizuseki, K.-R. Lee and A. K. Singh, *ACS Appl. Mater. Interfaces*, 2016, **8**, 24256–24264.
22 M. Tang, J. Li, Y. Wang, W. Han, S. Xu, M. Lu, W. Zhang and H. Li, *Symmetry*, 2022, **14**, 2232.
23 G. Li, S. Lian, J. Wang, G. Xie, N. Zhang and X. Xie, *J. Mater.*, 2023, **9**, 1160–1184.
24 J.-G. Liang and L. Pan, *Materials Nanoarchitectonics*, Elsevier, 2024, pp. 281–353.
25 Q. Zhou, L. Wang, W. Ju, Y. Yong, S. Wu, Y. Wang and H. Miao, *Colloids Surf., A*, 2023, **673**, 131870.
26 R. K. Choudhury, B. R. Bhagat, K. H. Mali, R. Pokar and A. Dashora, *Appl. Surf. Sci.*, 2022, **603**, 154426.
27 Z. Li, X. Cui, L. Jia, W. Zeng and Q. Zhou, *Diamond Relat. Mater.*, 2023, **139**, 110375.
28 R. P. Reji, S. K. C. Balaji, Y. Sivalingam, Y. Kawazoe and S. Velappa Jayaraman, *ACS Appl. Nano Mater.*, 2023, **6**, 5345–5356.
29 J. Su, X. Liu, H. Zhang, B. Zhao and T. Shen, *Micro Nanostruct.*, 2023, **183**, 207658.
30 K. Boonpalit, J. Kinchagawat, C. Prommin, S. Nutanong and S. Namuangruk, *Phys. Chem. Chem. Phys.*, 2023, **25**, 28657–28668.
31 X. Li, H. Wang, H. Li, Y. Chen, Y. Ni and Y. Xia, *Appl. Surf. Sci.*, 2023, **624**, 157125.
32 H. Dou, B. Yang, X. Hu, C. Huo, X. Wang and C. Shi, *Comput. Theor. Chem.*, 2021, **1195**, 113089.
33 B. Paul, R. Babarao and S. Kanungo, *Surf. Interfaces*, 2025, 106573.
34 L. Ju, X. Tang, X. Li, B. Liu, X. Qiao, Z. Wang and H. Yin, *Molecules*, 2023, **28**, 1644.
35 B. Babariya, D. Raval, S. K. Gupta and P. N. Gajjar, *Phys. Chem. Chem. Phys.*, 2022, **24**, 15292–15304.
36 J. P. Perdew, K. Burke and M. Ernzerhof, *Phys. Rev. Lett.*, 1996, **77**, 3865–3868.
37 B. Delley, *J. Chem. Phys.*, 1990, **92**, 508–517.
38 J. Wang, G. Wang and J. Zhao, *Phys. Rev. B: Condens. Matter Mater. Phys.*, 2002, **66**, 35418.
39 A. A. Piya, T. Ahmed, M. A. Khaleque, K. Ahmed and S. U. D. Shamim, *Comput. Theor. Chem.*, 2022, **1217**, 113902.
40 V. A. Basiuk and L. V. Henao-Holguín, *J. Comput. Theor. Nanosci.*, 2014, **11**, 1609–1615.
41 R. Pollet and H. Amara, *J. Chem. Theory Comput.*, 2009, **5**, 1719–1722.
42 S. Grimme, *J. Comput. Chem.*, 2004, **25**, 1463–1473.
43 J. Hu, Q. Zhang, Q. Zhang and H. Cui, *J. Mater. Res. Technol.*, 2022, **20**, 763–771.
44 T. Liu, Z. Cui, X. Li, H. Cui and Y. Liu, *ACS Omega*, 2020, **6**, 988–995.
45 H. Cui, X. Zhang, J. Zhang and Y. Zhang, *High Voltage*, 2019, **4**, 242–258.
46 S. U. D. Shamim, T. Akter, A. A. Ananna, B. K. Dash and A. A. Piya, *RSC Adv.*, 2025, **15**, 20712–20722.
47 S. U. D. Shamim, D. Roy, S. Alam, A. A. Piya, M. S. Rahman, M. K. Hossain and F. Ahmed, *Appl. Surf. Sci.*, 2022, **596**, 153603.
48 M. Amin, M. M. Rahman, M. K. Rokunuzzaman, M. K. Hossain and F. Ahmed, *Comput. Theor. Chem.*, 2024, **1242**, 114954.
49 K. N. Munny, T. Ahmed, A. A. Piya and S. U. D. Shamim, *Struct. Chem.*, 2023, **34**, 2089–2105.
50 T. Ahmed, A. A. Piya and S. U. D. Shamim, *Nanoscale Adv*, 2024, **6**, 3441–3449.
51 M.-Z. Liu, X.-H. Li, X.-H. Cui, H.-T. Yan, R.-Z. Zhang and H.-L. Cui, *Appl. Surf. Sci.*, 2022, **605**, 154830.
52 I. R. Shein and A. L. Ivanovskii, *Comput. Mater. Sci.*, 2012, **65**, 104–114.
53 M. H. Opi, T. Ahmed, M. R. Swarna, A. A. Piya and S. U. D. Shamim, *Nanoscale Adv.*, 2024, **6**, 5042–5054.
54 Y. Yong, H. Cui, Q. Zhou, X. Su, Y. Kuang and X. Li, *Appl. Surf. Sci.*, 2019, **487**, 488–495.
55 S. M. Aghaei, M. M. Monshi, I. Torres, S. M. J. Zeidi and I. Calizo, *Appl. Surf. Sci.*, 2018, **427**, 326–333.
56 Q. Hu, W. Liu, D. Li, Q. Wu, Y. Chang, J. Wang, Q. Xia, L. Wang and A. Zhou, *Mater. Today Commun.*, 2024, **40**, 109467.
57 E. Salih and A. I. Ayesh, *Phys. E*, 2021, **131**, 114736.
58 H. Y. Ammar, H. M. Badran and K. M. Eid, *Mater. Today Commun.*, 2020, **25**, 101681.
59 Y. Wu, X. Chen, K. Weng, J. Arramel, W. Jiang, P. Ong, X. Zhang, N. Zhao and N. Li, *Adv. Electron. Mater.*, 2021, **7**, 2001244.
60 J. Ren, W. Kong and J. Ni, *Nanoscale Res. Lett.*, 2019, **14**, 133.
61 A. S. Kharb, K. Kumar, A. K. Chawla and A. K. Mishra, *Phys. Chem. Chem. Phys.*, 2025, **27**, 9041–9055.
62 Y. Hu, L. Liu, S. Zhang and X. Chen, *Colloids Surf., A*, 2024, **689**, 133716.
63 K. Ma, J. Chen, X. Dai, J. Xiao, L. Wang, L. Xu and Z. Wang, *Results Phys.*, 2021, **28**, 104617.
64 Z. Wu, J. Zhou, D. Li, Z. Ao, T. An and G. Wang, *Sustain. Mater. Technol.*, 2021, **29**, e00294.
65 M. Mushtaq, N. Algethami, M. Abdul Rauf Khan, A. I. Ayesh, M. Mateen, A. Laref, S. A. M. Abdelmohsen and M. K. Hossain, *ACS Omega*, 2023, **8**, 14005–14012.
66 N. L. Hadipour, A. Ahmadi Peyghan and H. Soleymanabadi, *J. Phys. Chem. C*, 2015, **119**, 6398–6404.
67 A. A. Kistanov, Y. Cai, K. Zhou, S. V. Dmitriev and Y.-W. Zhang, *2D Mater.*, 2016, **4**, 15010.
68 R. Pohle, A. Tawil, P. Davydovskaya and M. Fleischer, *Proc. Eng.*, 2011, **25**, 108–111.